Flow regime identification in vertical upward gas-liquid flow using an optical sensor with linear and quadratic discriminant analysis

Kwame Sarkodie[1]

Division of Chemical and Energy Engineering, London South Bank University, London, UK

Department of Petroleum Engineering, Kwame Nkrumah University of Science and Technology, Kumasi, Ghana

PMB KNUST, Kumasi, Ghana

e-mail: sarkodik@lsbu.ac.uk, ksarkodie.coe@knust.edu.gh

Andrew Fergusson-Rees

Division of Chemical and Energy Engineering, London South Bank University

103 Borough Road, SE10AA, London, UK

e-mail: fergusa3@lsbu.ac.uk

Abstract

The accurate identification of gas-liquid flow regimes in pipes remains a challenge for the chemical process industries. This paper proposes a method for flow regime identification that combines responses from a non-intrusive optical sensor with linear discriminant analysis (LDA) and quadratic discriminant analysis (QDA) for vertical upward gas-liquid flow of air and water. A total of 165 flow conditions make up the data set, collected from an experimental air-water flow loop with a transparent test section of 27.3 mm inner diameter and 5-metre length. Selected features extracted from the sensor response are categorised into feature group 1, average sensor response and standard deviation, and feature group 2 that also includes percentage counts of the calibrated responses for water and air. The selected features are used to train, cross validate and test four model cases (LDA1, LDA2, QDA1 and QDA2). The LDA models produce higher average test classification accuracies (both 95%) than the QDA models (80% QDA1 and 45% QDA2) due to misclassification associated with the slug and churn flow regimes. Results suggest that the LDA1 model case is the most stable with the lowest average performance loss and is therefore considered superior for flow regime identification. In future studies, a larger data set may improve stability and accuracy of the QDA models, and an extension of the conditions and parameters would be a useful test of applicability.

Key words: *Two-phase flow measurement, non-intrusive, infrared sensor, machine learning, probabilistic, QDA*

1. Introduction

Two phase flow commonly occurs in pipes found across the chemical process industries such as the pharmaceutical and petroleum industries. These flows are observed as geometric distortions of the phases that occur due to variations in fluid fraction that can be classified into different flow regimes. Typical flow regimes that exist for a vertical upward flow include bubble, slug, churn and annular [1–4] . The complex nature of these flow regimes affects the accuracy of phase fraction and ultimately phase flow rate measurement. This leads to the requirement for the development of suitable flow regime identification methods. Optical sensors have been used successfully for the analysis of 2-phase flow in a number of previous studies [5–7]. This is due to the output voltage being proportional to the intensity of light detected. The severity of attenuation of the emitted light, due to scattering, refraction and absorption, is then a function of the two-phase flow regime. This principle makes the optical sensor provide a direct response to changes in flow regime [8].

Investigators have analysed sensor responses via statistical analysis methods to qualitatively and quantitatively infer flow regime. These include the probability density function (PDF) and the cummulative probability distribution function (CPDF) derived from pre-processed signals that reflect the phase fractions [5,9]. As an objective discriminator, the moments and turning points of the PDFs and CPDFs have not shown a global consistency, hence their limitation in identifying flow regimes as specified by [10]. Other discriminators have been developed based on the analysis of a frequency domain of a sensor response, commonly referred to as Fast Fourier Transform (FFT) and Wavelet Transforms (WT). These methods transform the temporal sensor responses into frequency domains where distribution of frequencies indicate flow regime effects [11,12]. However, the accuracy and consistency of developing an objective discrimination derived from these frequency features remains a challenge even though the energy of variance and entropies of these features have been considered specific to flow regimes effects [13].

Machine Learning (ML), as a branch of soft computing, is currently leading in pattern recognition and is suitable for the online identification of a large range of flow regimes without knowledge of the rate of flow. Brunton et al. [14] in their review of ML as applied to fluid mechanics mentioned that, “ML entails powerful information processing algorithms that are relevant for modelling, optimization, and control of fluid flows”. These developed

algorithms require features derived from typical sensor responses to solve classification problems using supervised and unsupervised learning.

Supervised learning is a ML task that derives functions based on a training data set with priori or labelled classifications which allocates observations to groups or classes of a new set of data or test data. In contrast, unsupervised learning is a self-learning ML task that develops functions that find hidden patterns in the training data set without priori or labelled classifications. The use of ML methods has shown improved accuracy over statistical and spectral methods [15,16]. Examples of these include regression, recurrence analysis, artificial neural network, cluster analysis, support vector machines and least square methods.

Sampling and cross validation methods provide understanding of model generalization and are considered as the convention for building robust models. Xu, and Goodacre, [17] provide details of the applicability of varied sampling and cross validation methods for supervised learning. However, certain issues remain a challenge, including sample insufficiency for training the algorithms; the requirement for numerous extracted input features; the complexity of hidden layers in assigning classes; and the optimization of fitting parameters. Dimensionality reduction methods, such as principal component analysis, have also been considered to reduce the numerous features into “feature spaces”, where further analysis can be carried out on the classification [18]. This may increase the number of steps required to build classification models, hence the need for more efficient classifiers.

1.1. Discriminant analysis

Discriminant Analysis (DA) is a form of supervised learning that encompasses methods of classification and dimensionality reduction [19,20]. The first and most commonly considered is Linear Discrimination Analysis (LDA), which can either be applied based on Fishers approach or the Bayes probabilities approach. Fishers approach (also known as Fishers Discriminant Analysis, FDA) tends to find the linear combination of features that maximizes the between-class variance relative to the within-class variance. Various researchers have considered FDA in other fields of study [21–23], however, few have applied FDA to multiphase flow studies. Ameel et al. [24] used FDA to reduce dimensionality of various features extracted from video footage of gas-liquid flow in a pipe. Li et al. [25] also successfully used FDA to identify flow regimes using responses from an array of optical sensors. The flow regime identification results were used to allocate valid void fraction models computed using support vector machines with a maximum error of 7 %.

The second interpretation of DA is a probabilistic view, which uses Bayes rule to determine a maximum posterior probability that discriminates between classes or groups based on priori probabilities of a training set. Wu et al. [26] mention that the use of probabilities as a classification criterion provides details about the separation distance of groups compared to the discrete classification accuracies from LDA. This enables the effect of sensor response extracted features to be assessed based on their classification accuracy. The probabilistic approach can also be applied to Quadratic Discriminant Analysis (QDA), which is a variant of LDA. It can be applied to cases where the covariances between groups are unequal. Although QDA computes more terms in the discriminant function, improvements in classification accuracies have been documented for larger data sets compared to LDA; Tharwat [22].

The probabilistic interpretation of DA has not been applied to multiphase flow classification based on literature search, particularly in the area of gas-liquid flow regime identification using a non-intrusive optical sensor. This provides the motivation to test the performance of LDA and QDA probabilistic approaches considering their classification accuracy for flow regime identification.

1.2. LDA and QDA formulation

LDA and QDA are derived from a probabilistic model that describes the class conditional distribution of the data $P(X|y=k)$ for observation X to class k. Predictions in the form of posterior probabilities $P(y=k|X)$ of each observation in a training set based on the priori probability $P(y=k)$ can be made using Bayes rule:

$$P(y=k|X) = \frac{P(X|y=k).P(y=k)}{P(X)} \tag{1}$$

The conditional distribution of the data can then be modelled as a multivariate Gaussian distribution with class mean μ_k:

$$P(X|y=k) = \frac{1}{(2\pi)^{d/2}|\Sigma_k|^{1/2}} \exp\left(-\frac{1}{2}(X-\mu_k)^t \Sigma_k^{-1}(X-\mu_k)\right) \tag{2}$$

where, d is the number of features, Σ_k is the class covariance matrix, and $(X-\mu_k)^t\Sigma^{-1}(X-\mu_k)$ is the Mahalanobis distance which computes the distance between the observation X and the class mean μ_k.

1.2.1. Linear Discriminant function

The posterior probability can be expressed in the form of the linear discriminant function when equal covariance matrices are assumed between class, such that $\Sigma_k = \Sigma$:

$$\log\ P(y = k|X) = -\frac{1}{2}(X - \mu_k)^t \Sigma^{-1}(X - \mu_k) + \log\ P(y = k) + Cst. \quad (3)$$

where, C_{st} corresponds to the denominator and other constant terms from the Gaussian expression in eq. (2).

1.2.2. Quadratic Discriminant function

For unequal class covariance matrices, the quadratic discriminant function defines the appropriate posterior probability for the allocation of observation *X* to class *k*:

$$\log P(y = k|X) = -\frac{1}{2}\log\ |\Sigma_k| - \frac{1}{2}(X - \mu_k)^t \Sigma_k^{-1}(X - \mu_k) + \log\ P(y = k) + Cst. \quad (4)$$

The QDA function in considered to provide more flexible decision boundaries compared to the linear decision surface of the LDA function, though this can also affect the stability of the model.

1.2.3. Performance assessment

The overall performance of each model case can be assessed, based on an average classification accuracy $\bar{A}_c$, which refers to the percentage of correctly classified observations to the total observations, weighted by the priori probabilities of each class *k*:

$$\bar{A}_c = (1 - \bar{e}_k) \quad (5)$$

where, $\bar{e}_k$ is the average class misclassification rate, or error rate, weighted by the class priori probabilities.

$$\bar{e}_k = \sum e_k\ .\ P(y = k) \quad (6)$$

2. Experimental set up

Figure 1 shows the schematic of the experimental flow rig set-up installed at the Chemical and Energy Engineering Laboratory, London South Bank University. The rig is designed to produce vertical upward flow of air and water and consists of a 5 m transparent PVCu test section (TS), of 27.3 mm internal diameter and wall thickness of 1.5 mm to aid the visual observation of the flow regimes.

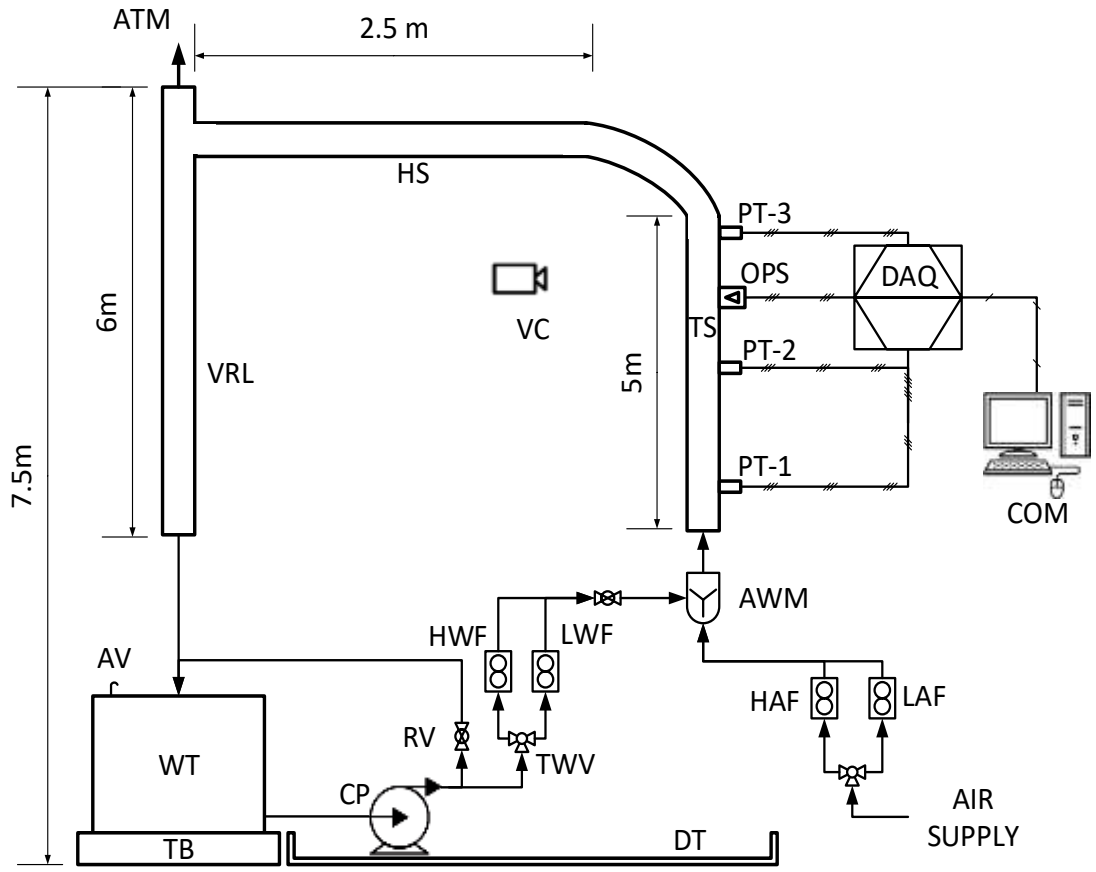

WT – Water Tank, AV – Air vent, TB – Tank Bund, CP – Variable speed centrifugal pump, RV – Return Valve, TWV – Three Way Valve, DT – Drip Tray, HWF – High Water Flowmeter, LWF – Low Water Flowmeter, AWM – Air-Water Mixer, HAF – High Air Flowmeter, LAF – Low Air Flowmeter, TS - Test Section, HS – Horizontal Section, VRL – Vertical Return Line, PT1,2,3 – Pressure Transducers, OPS – Optical sensor, DAQ – Data Acquisition Module VC – Video Camera, COM – Computer, ATM – Atmosphere

Fig. 1: Schematic of the air - water flow rig

Viewing Figure 1, air is delivered by compressed air supply at a discharge pressure of 6 bar, while the water is circulated from a 300 L water tank (WT) from Enduraxx, using an inline variable speed centrifugal pump set from Lowara (LPL10/10SV07). Water can be circulated to meet low flow rates (2 – 20 l/min) using a rotameter from Omega (FL-2080-V), designated

as LWF, and at high flow rates (19 – 190 l/min) using a turbine flow meter from pipe stock, designed as HWF. A three-way valve (TWV) is then used to select the desired flow path. The compressed air is also metered at low flow rates (5 – 100 l/min) and high flow rates (100 - 1400 l /min) using two rotameters both from Omega (FL-2017-SS and FL-2075-V) and designated as LAF and HAF respectively. Measurement uncertainties of air and water are determined to be +/-1.25% of the full-scale of each flow meter.

Water and air are injected to the bottom of the TS via an air water mixer (AWM), with air injected via a 4 mm pipe fitted with a non-return valve at the bottom of the TS. The optical sensor pairs (OPS) are installed non-intrusively at 180 D from the bottom of the TS. This ensures that fully developed flow regimes exist before the sensor, while negating bubble break up effects at the top bend of the TS. Data from the optical sensor is pre-treated and captured by the data acquisition module (DAQ) before being stored on a computer (COM) for further analysis. A NIKON, D300 video camera (VC), positioned at 5D from the TS and height of 180 D relative to the TS provides validation of the observed flow regimes to the sensor response. The VC can operate at a maximum rate of 60 frames per second and is fitted with a Godox V860 strobe light, to minimize ambient light effects on image quality. The captured photos are then stored on the computer and digitized using IMAGE J image processing software for flow structure measurement.

After the two-phase flow has circulated through the TS, it then passes through the horizontal section (HS) to the vertical return line (VRL), where air is separated and released to the atmosphere (ATM) and water is returned to the water tank for recirculation. Table 1 summarizes the range of flow conditions considered in this study. The superficial velocity of each phase v_{sl} and v_{sg} are calculated as a ratio of the volumetric flow rate Q to the cross-sectional area A_p of the test section pipe:

$$v_s = \frac{Q}{A_p} \tag{7}$$

Table 1. Summary of fluid conditions

Fluid	Density (kg/m^3)	Viscosity (cp)	Refractive index (-)	Surface tension (N/m)	Superficial velocity (m/s)
Water	998.00	1.00	1.33	0.0728	0 - 1.00
Air	1.20	0.00002	1.00	-	0 - 13.00

2.1. Optical sensor set up

Figure 2 presents a schematic of the optical sensor set-up showing its non-intrusive installation on the TS. The sensor (OPS-1 and OPS-2) consists of two pairs of light emitting diodes (LED-1 and LED-2) and light receiving photodiode (PD-1 and PD-2) from Balluf (BOH TJ-Q06-001-01-S49F) embedded in an opaque casing (OC). The LED emits infrared light at a wavelength of 1480 nm, which is then received by the photodiode, transmitted as a current signal, amplified by two signal amplifiers (SAC) from Balluf (BAE SA-OH-038-UA-DV02) and converted into a voltage signal. The output voltage is aquired using a two channelled data logger (DL) from Pico scope (model 2204), at a rate of 3000 Hz for periods of 60 seconds per flow condition.

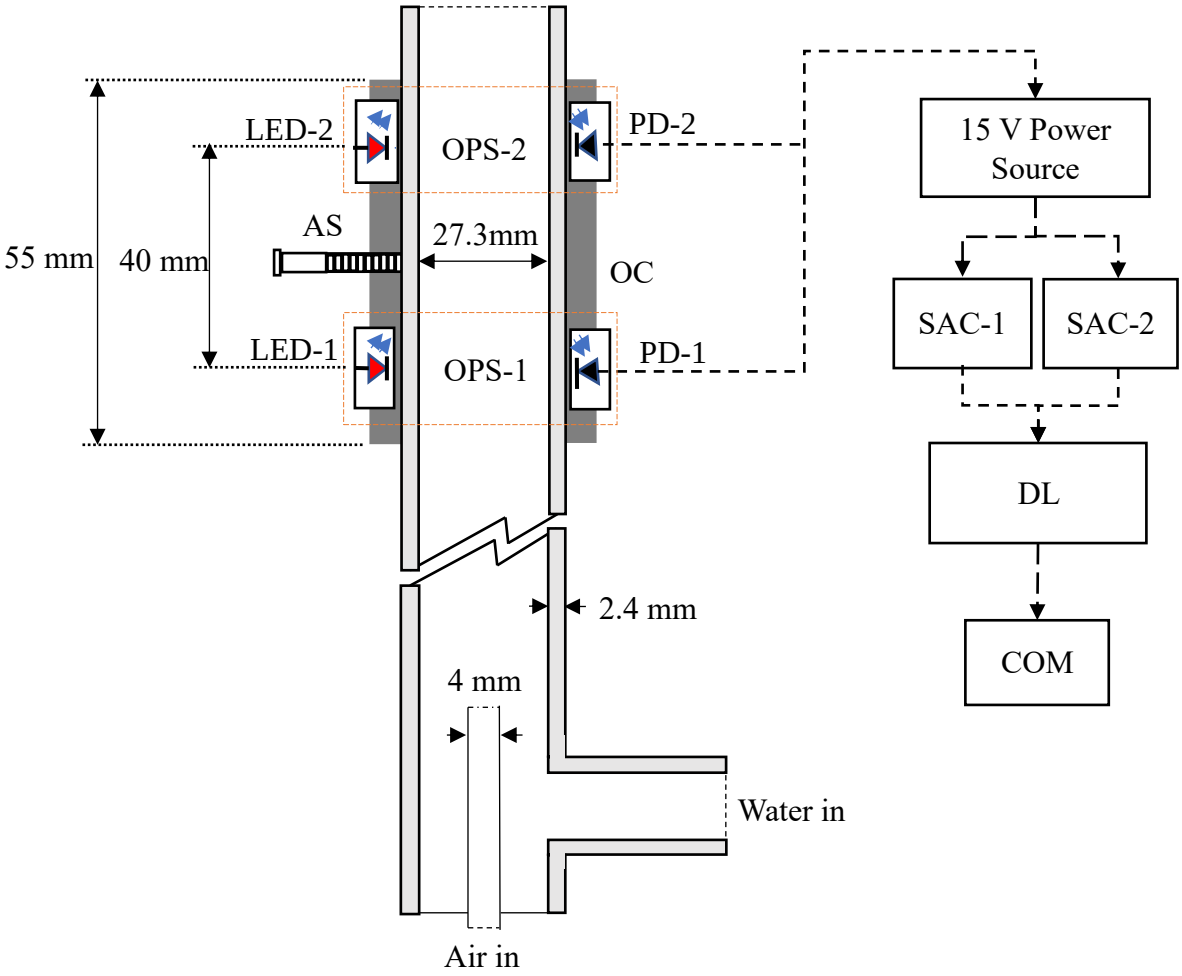

OPS-1 – Bottom Optical Sensor Pair, OPS-2 – Top Optical Sensor Pair, LED-1 – Bottom Light Emitting Diode, LED-2 – Top Light Emitting Diode, PD-1 – Bottom Photodiode, PD-2 – Top Photodiode, AS – Adjusting Screw, OC – Opaque Casing, SAC-1 – Signal Acquisition and Conditioning for bottom sensor, SAC-2 – Signal Acquisition and Conditioning for top sensor, DL – Data logger, COM – Computer

Fig. 2: The setup of the non-intrusive optical sensor.

2.2. Sensor calibration

To calibrate the sensor, the test section was initially air-filled and then water injected at a low rate creating a moving interface. Figure 4 shows the drop from V_{air} to a steady V_{water}. The results presented in figure 3 show that a lower response is captured in the presence of a water-filled pipe (V_{water}) compared to the higher response for the presence of an air-filled pipe (V_{air}). This disparity in response relates to the higher absorption coefficient of water relative to air at the wavelength of 1480 nm as supported by literature. Therefore, these results present an adequate detection for the presence of water and air. The effect of the air-water interface on the sensor response is also identified as the minimum voltage (V_{int}). This drop is due to the moving interface which acts as a barrier or mirror, and scatters the emitted light, hence producing a low voltage response V_{int}. Table 2 summarizes the responses for both sensor pairs (OPS-1 and OPS-2) after the calibration process.

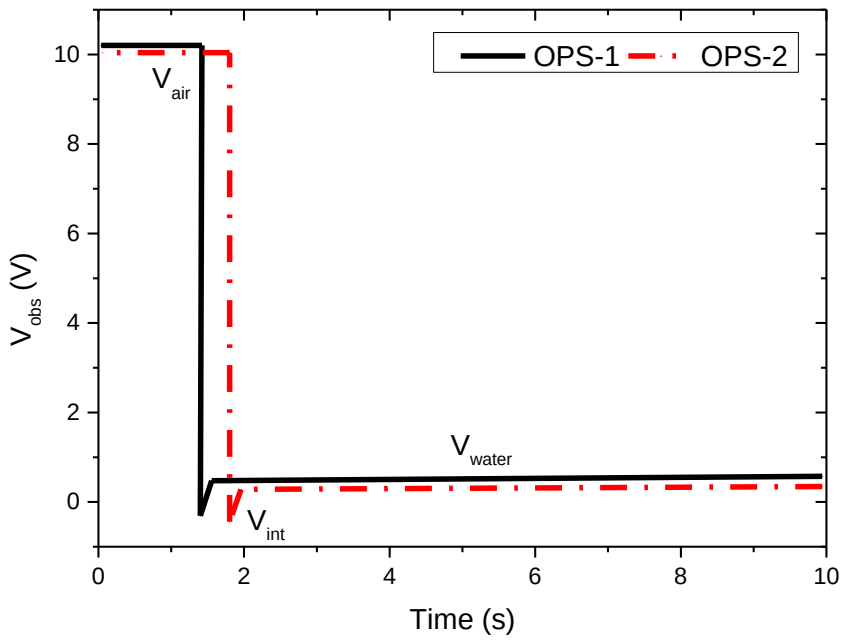

Fig 3: Sensor calibration showing typical bottom sensor OPS-1 and top sensor OPS-2 response to the presence of an air and then water filled test section.

Table 2. Summary of sensor response to water, air and interface

Response (V_{obs})	**OPS -1**	**OPS -2**
V_{water}	1.18	0.68
V_{air}	10.25	10.20
V_{int}	-0.07	-0.03
Deviation σ (+/-)	0.0010	0.0010

To maintain computational consistency, the OPS-1 pair was used for all further analysis. OPS-2 was only used to verify that the flow structures were of similar geometry in the sensing area.

3. Flow regime identification

The flow regime identification approach considered here, follows five key steps, illustrated in figure 4, associated with the development of classification models based on works by [21,23]. The implementation of the DA algorithms for training, cross validation and testing can be carried out using the built-in functions in Scikit-Learn with Python programming in a Google Collaborator environment.

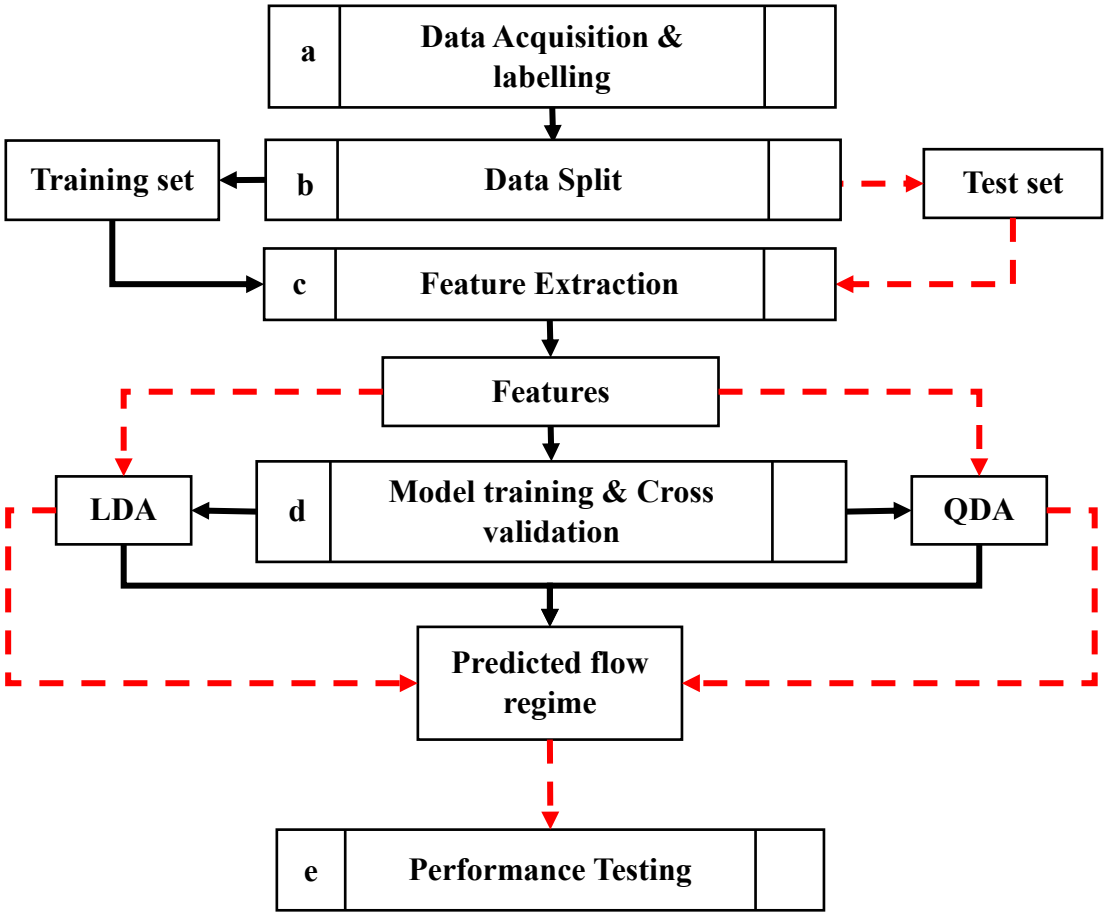

Fig. 4: The flow regime identification approach

a. **Data Acquisition and labelling -** Data in the form of voltage- time series (V_{obs} (t)) is acquired from the sensor for a set of flow conditions, (v_{sl}; 0. – 1.0 m/s and v_{sg}; 0 – 13.0 m/s), which cover the bubble, slug, churn and annular flow regimes. The data sets derived from each flow condition are then labelled or allocated to a flow regime based on visual observation and the video camera output, with the transitions between flow regimes validated using a flow regime map [27].
b. **Data split -**The labelled data sets are randomly split into a training set that makes up 88% of the data and a test set of the remaining 12%. The training set is selected to model the decision boundaries of each DA model, termed as model fitting and used to cross validate the models, while the test set is used to evaluate the predictive performance of each model case.
c. **Feature extraction and selection -** Statistical analysis of the training set is performed to extract features required as inputs for model training. The selection of relevant features is achieved based on the correlation of each feature with the homogenous gas fraction defined as, $\beta = \frac{v_{sg}}{v_{sg}+v_{sl}}$. Feature extraction of the selected features is also performed on the test set required for model performance assessment. Each selected feature is then normalized based on the maximum possible value of each feature.
d. **Model training and cross validation -** The selected features extracted from the training set are used to fit each model case of the LDA and QDA using the appropriate functions described in eq. (3) and (4) respectively. In order to understand the generalization or stability of each model case, a leave one-out cross validation (LOOCV) is performed on the trained models. The LOOCV is considered for this study due to its suitability for small training data sets. A comparison of the training and cross validation accuracies helps to interpret model stability or robustness, with the most stable model cases expected to present the lowest error difference or loss.
e. **Performance Testing –** The performance of each model case for the prediction of the test data (unknown to the trained models) is considered with a comparison of the average classification accuracy specific to each flow regime classification.

4. Results and discussion

4.1. Data Acquisition

A total of 162 data sets are presented for water and air superficial velocities ranging from 0 – 1 m/s and 0 – 13 m/s respectively, within the test section. The data sets represent the sensor response captured in the presence of the bubble, slug, churn and annular flow regimes, with associated transitions. The effect of increasing gas fraction β on the optical sensor response with regards to flow regime identification is discussed.

4.1.1. Bubble flow

The presence of bubble flow as presented in the photograph of figure 5 (at β = 0.13, v_{sl} = 0.86 m/s and v_{sg} = 0.13 m/s) is characterised by the presence of spherical (around 4 mm) and ellipsoidal (4mm – 10 mm) bubbles dispersed in the liquid. Investigations by [28–30] indicate that the formation of ellipsoidal bubbles in vertical flow is due to the balance of drag and buoyancy forces at a given rise velocity. The corresponding sensor response (figure 5), is characterized by two ranges of signal variation created by the gas-liquid interfaces. The first is variation within the V_{water} and V_{int} responses due to smaller spherical bubbles. The second is variation between the V_{int} and V_{air} responses due to larger ellipsoidal bubbles. The ellipsoidal bubbles tend to admit a higher intensity of light to be received by the photodiode, hence the increase in response from V_{int} to V_{air}. Dutra et al. [31] observed similar responses and termed it the lensing effect.

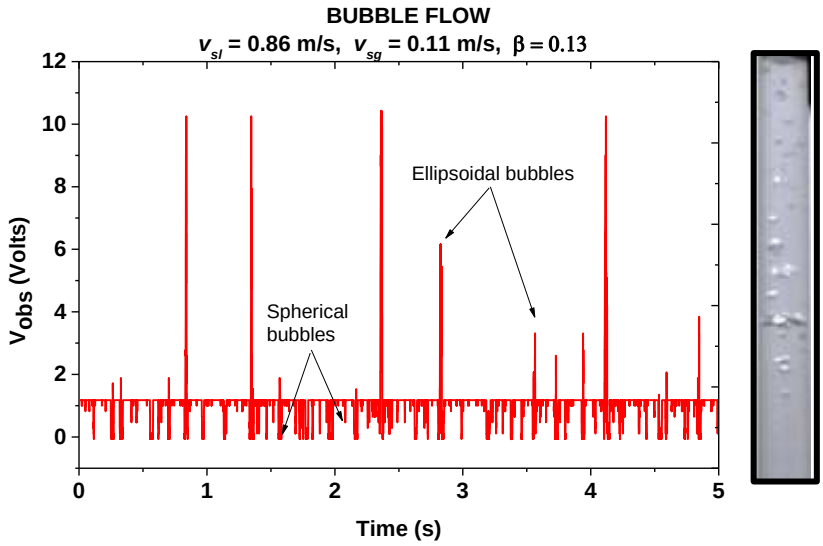

Fig. 5: Typical sensor responses with corresponding photos for bubble flow at β = 0.13

4.1.2. Bubble – Slug transition

Further increase of the gas fraction (β > 0.27), produces a transition from bubble to slug flow regime. This transition occurs due to the coalescence of ellipsoidal bubbles into larger bubble caps with diameter approaching that of the pipe (figure 6 photograph). This coalescence mechanism has been reported to be significantly dependent on the bubble size, void fraction waves and turbulence of flow [32–34]. The sensor response from figure 6 (β = 0.29, v_{sl} = 0.69 m/s and v_{sg} = 0.26 m/s) indicates variations between calibrated responses (i.e. V_{int}, V_{water} and V_{air}), however, the increase in the residence time of the V_{air} response representing the short lengths of the bubble caps (equivalent to pipe diameter) can be observed.

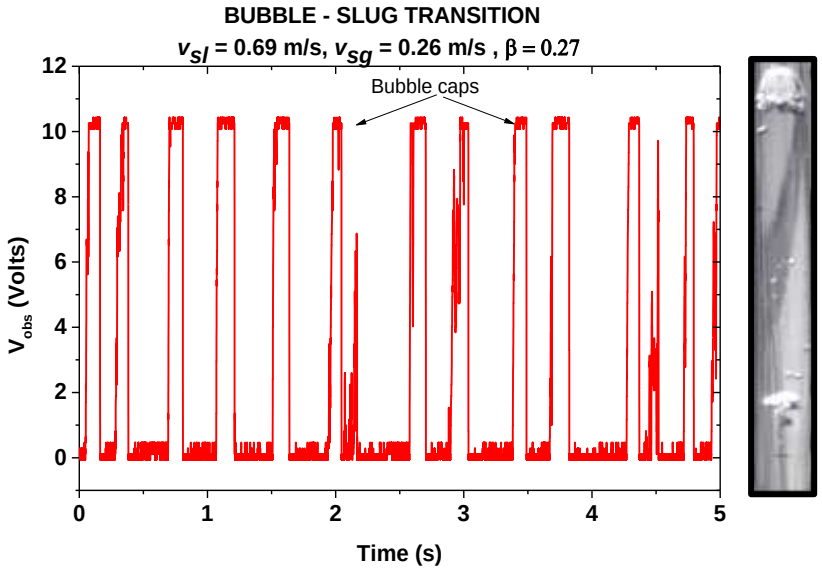

Fig. 6: Typical sensor responses with corresponding photos for bubble-slug transition at β = 0.27.

4.1.3. Slug flow regime

The photograph in figure 7 (β = 0.61, for v_{sl} =0.49 m/s and v_{sg} = 0.78 m/s) shows the presence of a slug flow regime, characterized by the presence of rising Taylor bubbles with diameters close to that of the pipe and lengths increasing to a maximum of 10 D. The bubbles are separated by liquid slugs with entrained spherical bubbles carried in the wake of the Taylor bubbles, hence forming an intermittent pattern of flow. It can be seen that the corresponding signal response in figure 7 shows longer residence times for $V_{air,}$ compared to the bubble caps detected in figure 6, which is due to the longer bubble lengths present. Consequently, a stable response of V_{air} and V_{water} infers the Taylor bubble and liquid slug lengths respectively.

Signal scattering between V_{int} and V_{water} indicates the presence of the entrained bubbles in the liquid slug.

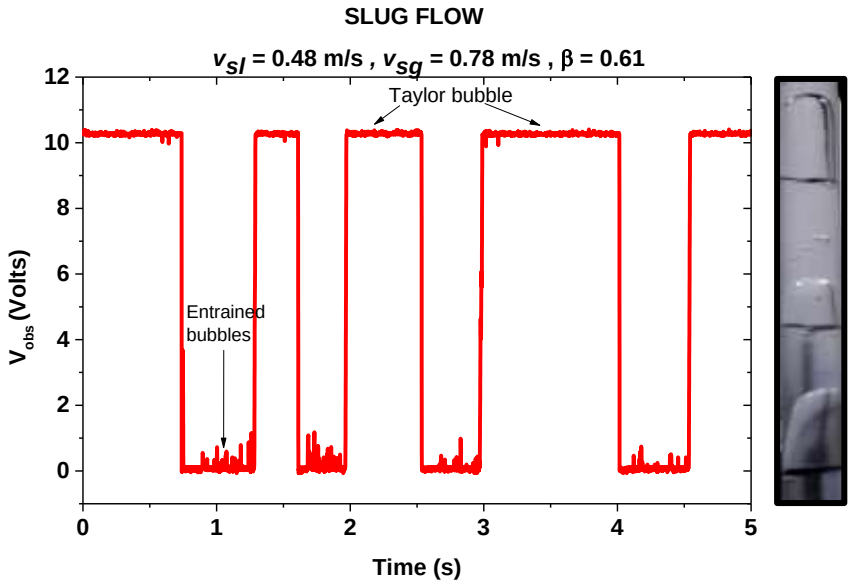

Fig. 7: Typical sensor responses with corresponding photos for slug flow at β = 0.61

4.1.4. Slug-churn transition

A transition from slug flow to churn flow is observed to occur at approximately β > 0.8. The underlining consequence of the higher gas fraction leads to the reduction of the liquid slugs separating the Taylor bubbles. This further leads to Taylor bubble instability since the entrained bubbles in the liquid slugs coalesce, destroy the slugs and Taylor bubble noses. Brauner and Barnea [35] describe this mechanism as the coalesce effect. Costigan and Whalley [36] also observed similar instability of bubbles at high gas fractions and refer to this as an unstable slug flow. Figure 8 (at β = 0.83, v_{sl} = 0.20 m/s, v_{sg} = 1.04 m/s) shows an unstable Taylor bubble and its corresponding sensor response indicating the bubble break up and reduced residence time of the V_{water} response, inferring a reduction of the liquid slug. Response variations at 0 – 0.5s and 2.5 – 3s indicate turbulence of entrained bubbles which tend to break up the liquid slugs.

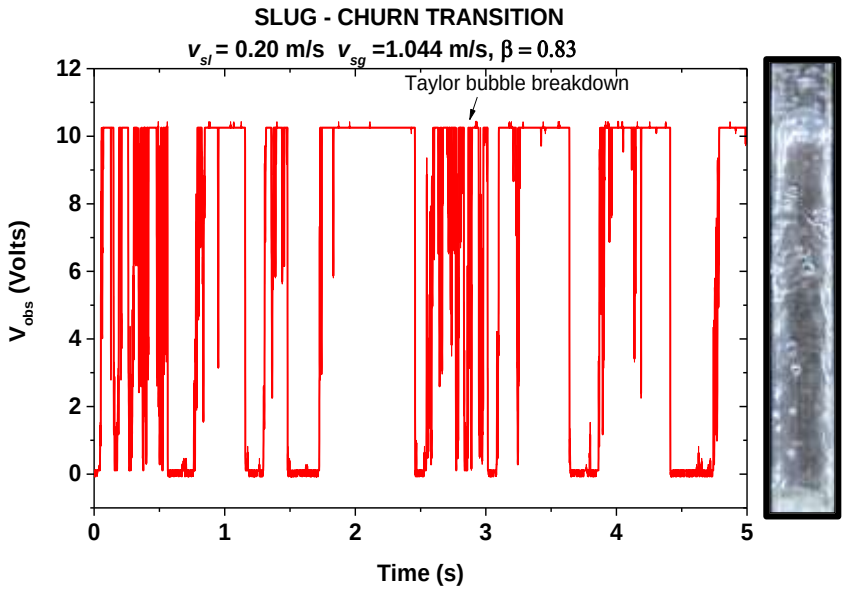

Fig. 8: Typical sensor responses with corresponding photos for slug – churn transition at β = 0.83

4.1.5. Churn flow regime

Beyond the observed slug to churn transition, a chaotic flow termed the churn effect by many researchers can be observed in figure 9 (β = 0.89, v_{sl} = 0.23 m/s v_{sg} = 1.83 m/s). This occurred at higher gas fractions where the breakdown of the liquid slug prevented the formation of Taylor bubbles. The corresponding sensor response in figure 9 further shows significant scattering compared to the response in figure 8. This indicates turbulence due to bubble break up and interfacial effects.

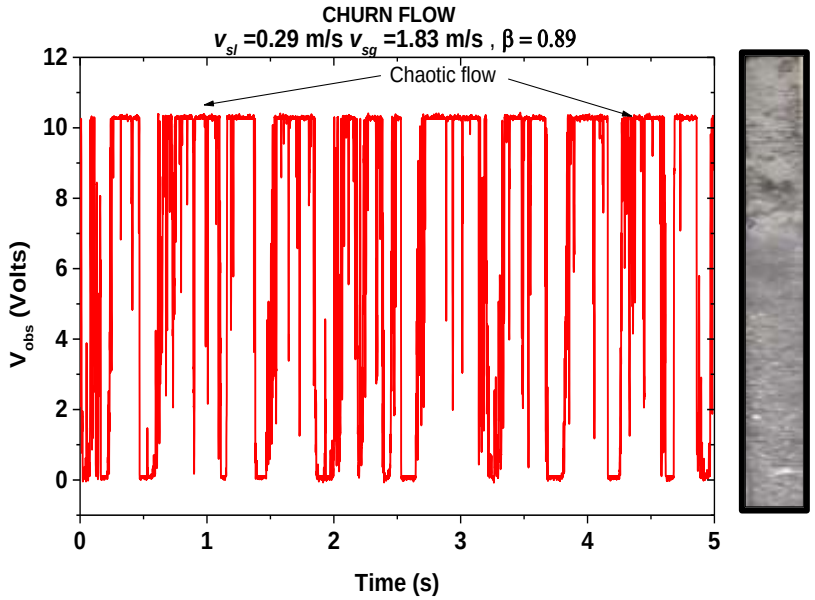

Fig. 9: Typical sensor responses with corresponding photos for churn flow at β = 0.89

4.1.6. Annular flow regime

Figure 10 shows a typical sensor response for annular flow in the test section (β = 0.98, v_{sl} = 0.11 m/s, v_{sg} = 5.22 m/s). A steady response around V_{air} can be observed with minimal interfacial effects produced by the rising liquid film, which leads to drops in response around V_{int}. The presence of entrained liquid droplets presents as attenuations within the $V_{air} < V_{obs} < V_{water}$ range, since the droplets are not large enough to be captured as a full V_{water} response. It was observed that the entrained liquid droplets are formed based on extreme deformation of the liquid film. Waves created at the gas-liquid film interface by hydrodynamic and surface tension forces result in wave breakup into several droplets [37,38]. The photograph (to the right) in figure 10 shows the wavy liquid film, with a continuous gas core at the centre of the test section.

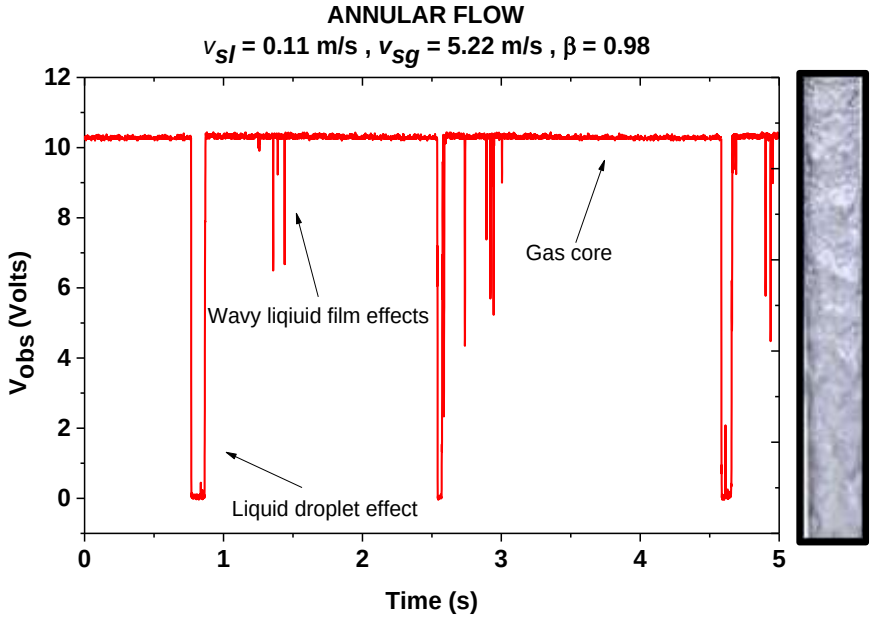

Fig. 10: Typical sensor responses with corresponding photos annular flow at β = 0.98

4.2. Data set labelling

Flow regimes are allocated to each of the 165 flow conditions based on the results of the sensor response and validation from photographs. The allocations are also compared to other works in literature in the form of a composite flow map, since a visual observation can be subjective. In context, a composite flow map refers to a plot of varied transition criteria from different investigators that define flow regime transition boundaries.

Wu et al. [27] present a composite flow map based on 2500 experimental data points, which uses the three most reliable transition models from literature to describe flow transitions of an upward vertical flow of air and water for a pipe size range of 10–50 mm. The transition models include the bubble-slug (B-S) model by [32], slug-churn (S-C) model by [39] and churn-annular (C-A) model by [1]. In the current study, the assigned flow regimes agreed with the composite flow map boundaries as shown in figure 11 for all 165 flow conditions, given that the bubble cap region was taken as a bubble flow, slug-churn transition as a churn flow and churn-annular transitions as annular flow.

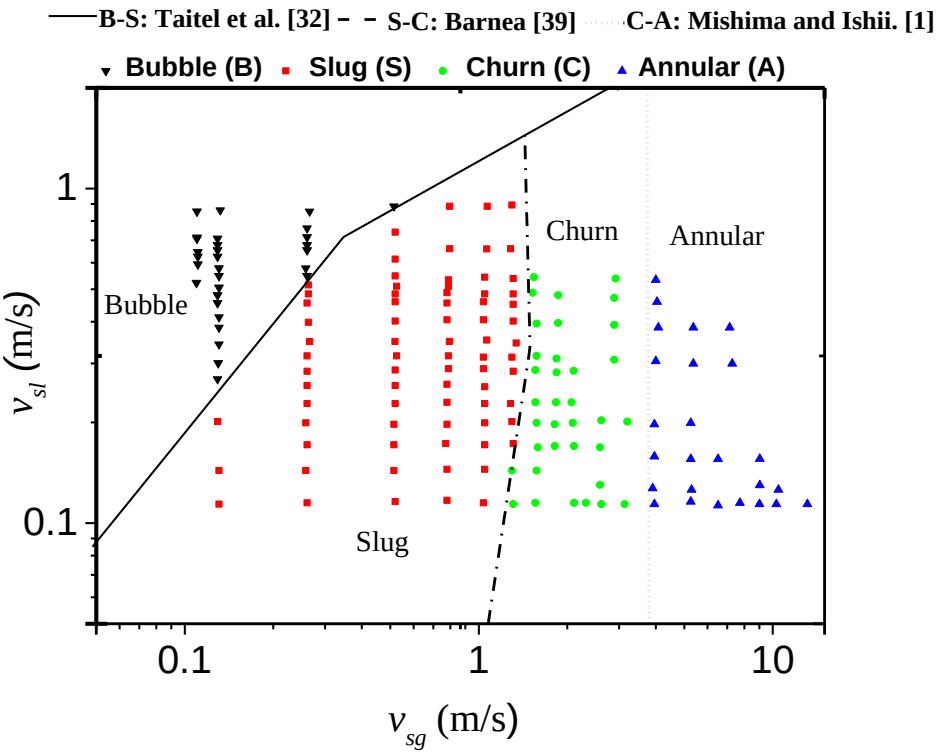

Fig. 11: Comparison of the labelled flow regimes for all 165 flow conditions showing agreement with the modified composite flow map by Wu et al. [27].

4.3. Data split

The data set split involved the random selection of the training and test data sets based on a ratio of 88:12, which translates to an equivalent of 145 training and 20 test data sets. Figure 12 explains the random selection procedure of the test data sets implemented via the RAND function in Microsoft Excel. A distribution of observations of the data set categories is also summarized in table 3.

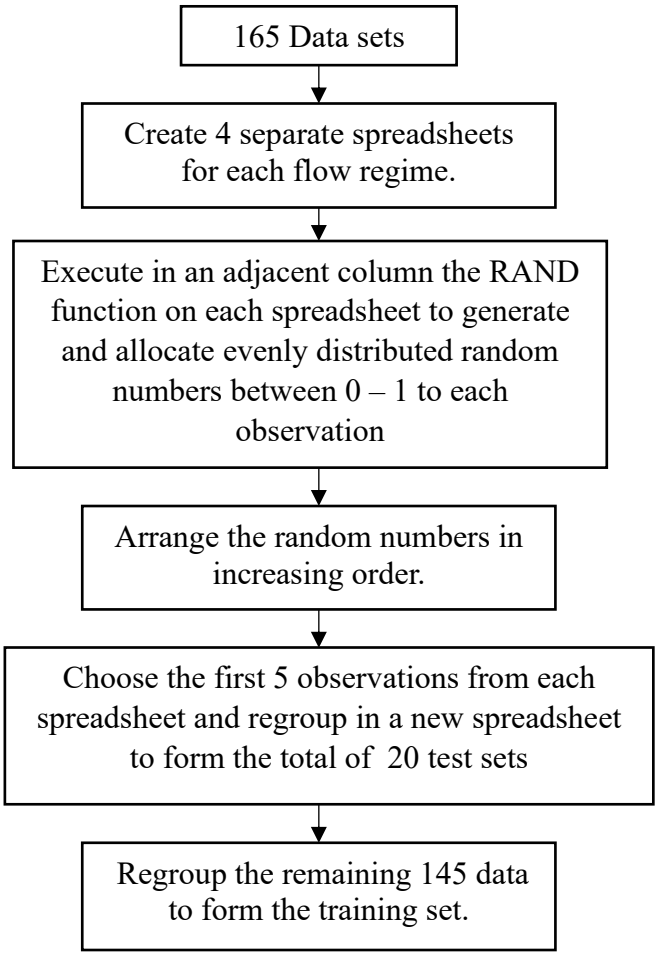

Fig. 12: Flow chart of the random selection procedure of the test data set and training set

Table 3. Summary of assigned flow regimes for the training, and test data sets

	Data set	Training set		Test set	
Flow regime	Observations	Observations	Data range	Observations	Data range
Bubble	30	25	1 - 25	5	1 - 5
Slug	76	71	26 - 96	5	6 - 10
Churn	34	29	97 - 125	5	11 -15
Annular	25	20	126 - 145	5	16 - 20
Total	165	145		20	

4.4. Feature extraction

Five features can be extracted from the sensor response ($V_{obs}(t)$) for analysis. These include: the average sensor response $\bar{V}_{obs}$; standard deviation, σ_{sensor}; and the percentage count of the calibrated sensor responses $\%\, V_{water}$, $\%\, V_{air}$ and $\%\, V_{int}$. The average sensor response $\bar{V}_{obs}$, and standard deviation σ_{sensor} are computed based on a time average for each flow condition using equations (8) and (9) respectively.

$$\bar{V}_{obs} = \frac{1}{N}\sum_{i=1}^{N} V_{obs} \tag{8}$$

$$\sigma_{sensor} = \sqrt{\frac{1}{N-1}\sum_{i=1}^{N}(V_{obs} - \bar{V}_{obs})^2} \tag{9}$$

The percentage counts of the calibrated responses ($\%\, V_{water}$, $\%\, V_{air}$ and $\%\, V_{int}$.) are computed as a percentage of the number of captured calibrated sensor responses (N_{water}, N_{air}, N_{int}) to the total number of data points N, captured by the sensor .

$$\%\, V_{calibrated\ response} = \frac{1}{N}\sum_{i=1}^{N} N_{calibrated\ response} \times 100 \tag{10}$$

According to [40], adequate feature selection involves the choice of useful features that provide unique discriminatory information, hence eliminating noisy features that only provide unexplainable variance in the model. This leads to the requirement for screening of the features that provide clear trends and correlation to gas fraction.

4.5. Feature screening

Figure 13(a-e) presents results of the extracted features and their relationship with the gas fraction for the training set.

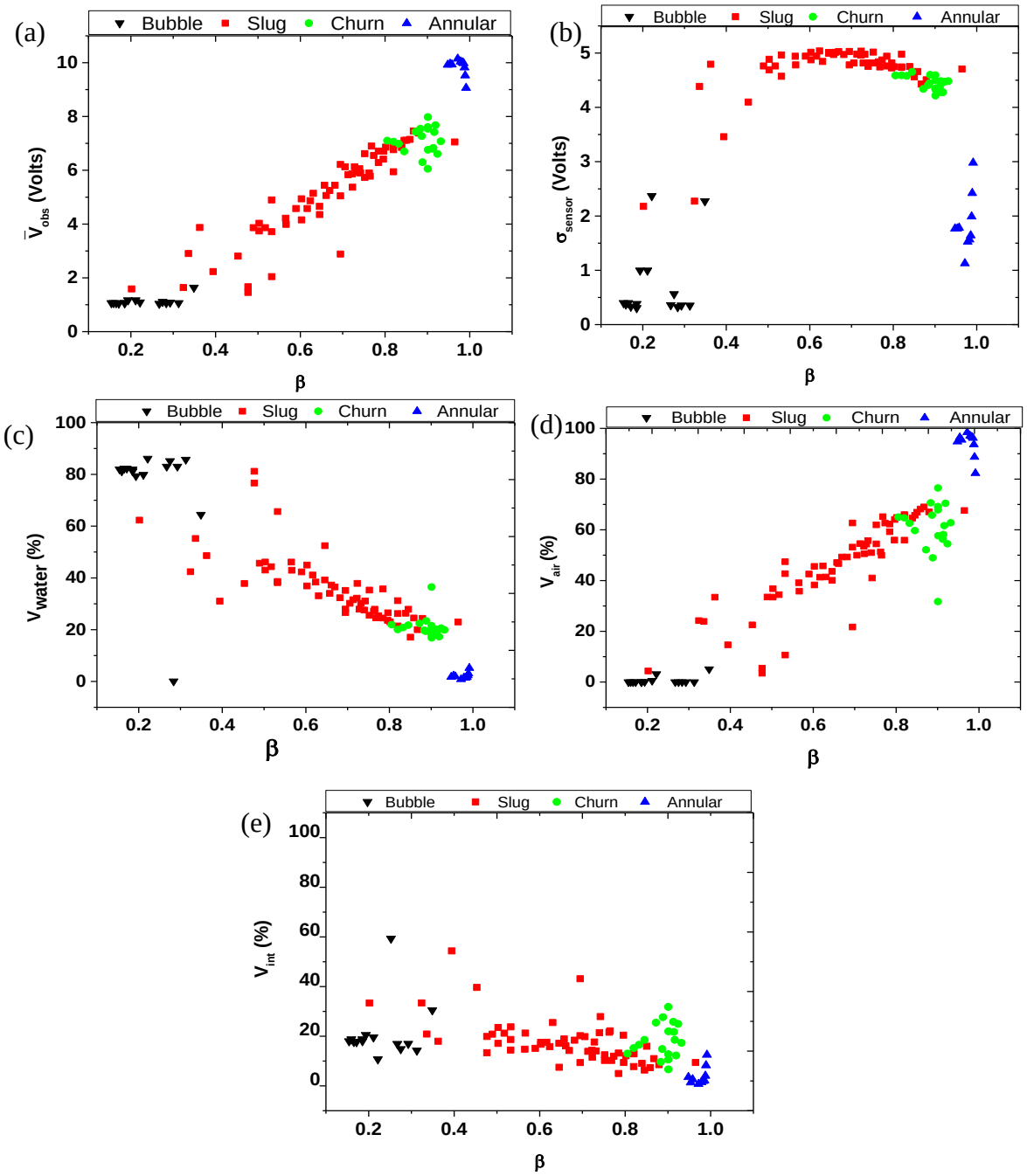

Fig. 13: Plots of the extracted features from the sensor response of the training data set showing the effect of gas fractions and flow regime on the (a) $\bar{V}_{obs}$ (b) σ_{sensor} (c) % V_{water} (d) % V_{air} (e) % V_{int}

Average sensor response

Figure 13(a) presents the result of the effect of gas fraction β on the average sensor response $\overline{V}_{obs}$ for the training data set. The results show a general linear trend for most of the data points corresponding to the slug flow regime. This trend is due to an increase in Taylor bubble lengths causing an increase in light received by the sensor. For the bubble flow regime, an increase in β produces a slight variation in $\overline{V}_{obs}$ within 1.1V, which is indicative of the presence of smaller bubbles (spherical and ellipsoidal bubble) interfacial scattering. It also follows that the smaller bubbles do not coalesce within this region, but rather form clusters which produce varied levels of scattering, hence the variation in $\overline{V}_{obs}$. At approximately β = 0.3 an abrupt transition from bubble to slug flow is evident and indicative of the sudden formation of bubble caps due to the clustering and coalescence of smaller bubbles. At higher average sensor responses beyond 6.9 V and β = 0.8, a deviation from the apparent linear slug trend can be observed due to the slug-churn flow transition. The slight reduction in average sensor response is simply due to interfacial scattering and bubble break down as previously discussed. At gas fractions greater than 0.9, a general increase in $\overline{V}_{obs}$ is observed in the annular region due to reduced scattering effects, attributed to variations in the liquid films thickness and the presence of entrained liquid droplets in the gas core.

Sensor standard deviation

The σ_{sensor} is a feature that represents fluctuations in the sensor response caused by the flow structures in each flow regime. Figure 13(b) presents the results of the effects of β on σ_{sensor}. The bubble flow regime data points show fluctuations in the sensor response due to the effects of scattering similar to that observed in figure 13(a). However, the variation is amplified using the standard deviation thus providing unique discriminatory information. In the range of, $0.3 < \beta < 0.6$, a general increase in σ_{sensor} can be observed corresponding to the bubble-slug transition (bubble cap formation) and the development of slug flow (Taylor bubble formation). A decrease in rate of increase in σ_{sensor} as β approaches 0.6 infers the formation of the maximum stable bubble length, which corresponds to the maximum fluctuation in response of 5 V. Further increase in the gas fraction ($0.6 < \beta < 0.9$) leads to a decreasing trend in response fluctuation indicative of bubble breakdown and the churn flow transition. Above gas fractions of 0.9, the annular flow regime produces a lower fluctuating response due to the reduced changes in the flow structure.

Percentage counts of calibrated responses

The relationship between gas fraction and the percentage count of calibrated responses is presented in figures 13(c), (d) and (e). The $\%\, V_{water}$ plot in figure 13(c) shows a general reduction for increase in gas fraction. The scattering of data for the bubble-slug transition is indicative of variations in light scattering due to bubble cap formation in the bubble flow regime. The $\%\, V_{water}$ drops markedly for the annular flow regime due to the presence of only the thin liquid film. The $\%\, V_{air}$ also in figure 13(d) shows an inverse trend compared to the $\%\, V_{water}$ for increase in gas fraction. The $\%\, V_{int}$ plot in figure 13(e), shows a lack of any distinct correlation, given the consistent range of data scatter for increase in the gas fraction. This is related to the complex interfacial interactions between the gas and liquid phase in the form of bubble movement, Taylor bubble growth, unstable Taylor bubble breakdown and the wavy liquid film in the annular flow regime.

4.6. Feature selection

Based on the analysis of results in figures 13(a-e) the average sensor response, and standard deviation are selected as the key features for training the DA models, since these features provided unique discriminatory information indicative of variations in flow regime. The combination of both features form feature group 1. Feature group 2 combines feature group 1 with $\%\, V_{water}$ and $\%\, V_{air}$. The $\%\, V_{int}$ feature not selected since it does not provide a clear trend unique to each flow regime. Table 4 summarizes the selected feature groups required for the training of the LDA and QDA models.

Table 4. Selected feature groups

Group	Feature	Model
1	$\bar{V}_{obs}$ and σ_{sensor}	LDA1 and QDA1
2	$\bar{V}_{obs}$, σ_{sensor}, $\%\, V_{water}$ and $\%\, V_{air}$	LDA2 and QDA2

A max-min normalization was performed on each feature to provide consistent scales prior to the training process:

$$x_{i\,norm} = \frac{x_i - x_{\,min}}{x_{\,max} - x_{\,min}} \tag{11}$$

where, x_{norm} is the normalized feature, x_i represents the value of each feature and $x_{\,min}$ and $x_{\,max}$ are the minimum and maximum feature values for the data sets.

4.7. Model training

The model training process involved the use of the selected features derived from the 145 training data sets as vector inputs, to develop decision boundaries of the LDA and QDA model cases. Figure 14(a-d) presents results of the computed posterior probabilities for each DA model case, with each observation allocated to a flow regime based on the maximum posterior probability. The posterior probability is also an indication of the separability of each observation from a decision boundary described by each discriminant function. The effects of model complexity and feature groups on separability are discussed.

(a)

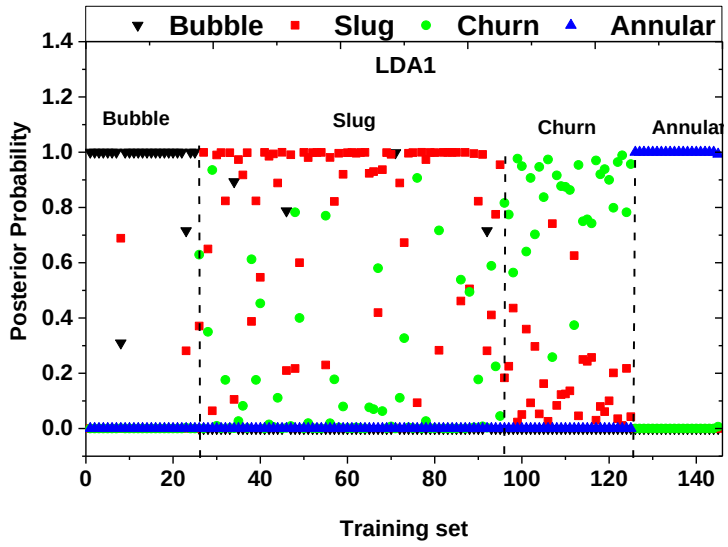

(b)

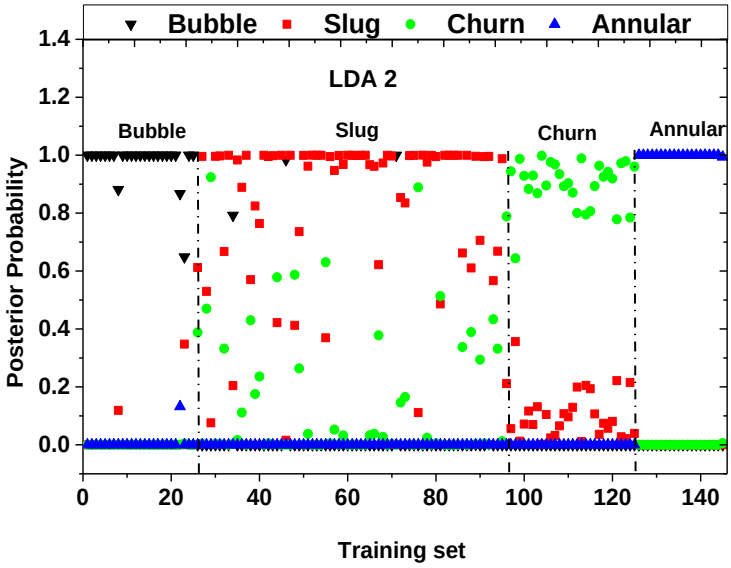

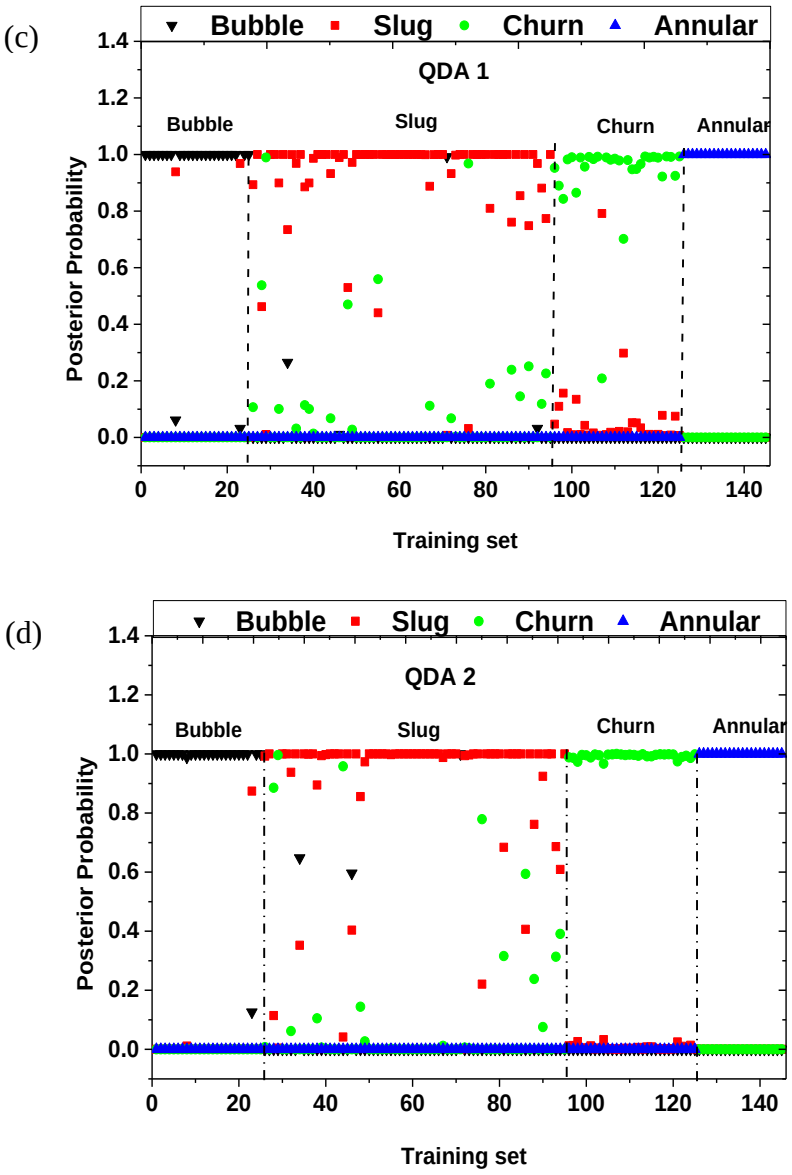

Fig. 14: Posterior probability plots of the training data set for the (a) LDA1 (b) LDA2 (c) QDA1 (d) QDA2.

A visual inspection of the computed posterior probabilities in figure 14(a-d), shows clear separation for most observations in the bubble flow (1-25), churn flow (97-125) and annular flow (126-145) ranges for all DA cases. A clear distinction of flow structures and features among the bubble, churn and annular flows, as previously described, is the reason for this separation. Within the slug flow data range (26 – 96) of the LDA model cases in figures 14(a) and 14(b) respectively, poor separation can be observed between the slug and churn flow regimes compared to the QDA model cases in figures 14(c) and 14(d) respectively.

This disparity in separation is indicative of the less distinctive input features that result from the apparent structural similarity between the slug and churn flow regimes at flow transition conditions. In effect, the linear decision boundaries of the LDA model cases are less flexible in defining adequate separation at the transition regions. On the other hand, the QDA model cases provide better separation of the slug-churn flow transition since each model is defined by a quadratic decision function, which provides more flexible decision boundaries.

The effect of the feature groups on the computed posterior probabilities can also be observed in figure 14. The Inclusion of the percentage counts of V_{air} and V_{water} from feature group 2 provides better separation of the posterior probabilities, since each feature adds unique discriminatory information to each model. This effect can be observed by the comparison of LDA1 with LDA2, figures 14(a) and (b) respectively, and QDA1 with QDA2, figures 14(c) and (d) respectively. However, it is important to note that better separation of probabilities may be related to the nature of the DA functions and may not always translate to an improvement in the performance of the DA model cases.

Table 5 presents a summary of the training performance metrics for each DA model case. According to the training average classification accuracy, it can be observed that the LDA1, LDA2, QDA1 and QDA2 performed at 87.59%, 93.10%, 93.79% and 93.10% respectively. A higher training performance by the LDA2 relative to LDA1 is related to the increase in feature inputs, which decreases the bias-variance ratio of the linear functions, hence a better model fit on the training data set. However, the increase in feature input of the QDA model case produces a slight decrease in training average classification accuracy, which is indicative of an increase in model variance and may infer a state of overfitting by the QDA2 model case.

Overall, the training performances of the DA model cases indicate an adequate and acceptable potential to identify flow regimes compared to other investigations [22–24,41]. To further ascertain this claim, subsequent cross validation and testing of each model case is presented.

Table 5. Summary of training performance metrics

Model case	Metrics	Flow regimes				Weighted Average $(\bar{e}_k, \bar{A}_c)$
		Bubble	Slug	Churn	Annular	
LDA1	e_k	4.00	21.13	6.90	0.00	12.41
	A_c	96.00	78.87	93.10	100.00	87.59
LDA2	e_k	0.00	14.08	0.00	0.00	6.90
	A_c	100.00	85.92	100.00	100.00	93.10
QDA1	e_k	8.00	8.45	3.45	0.00	6.21
	A_c	92.00	91.55	96.55	100.00	93.79
QDA2	e_k	4.00	12.68	0.00	0.00	6.90
	A_c	96.00	87.32	100.00	100.00	93.10

4.8. Model cross validation

The LOOCV of the trained DA models can be performed to investigate model stability and dependence on the training set. The LOOCV is performed with n-1 of the training sets used to fit the models and one data set left out and used as a validation set. The validation is then run n times with an average cross validation classification accuracy computed. After the cross validation of each model case, the difference, referred to as the loss between the training and cross validation performance metrics is used to infer model stability. The loss is therefore understood as inversely proportional to model stability. A summary of the cross-validation performance results is presented in table 6.

Table 6. Summary of cross validation performance metrics

Model Case	Metrics	Flow Regimes				Weighted Average $(\bar{e}_k, \bar{A}_c)$
		Bubble	Slug	Churn	Annular	
LDA1	e_k	4.00	22.54	6.90	0.00	13.10
	A_c	96.00	77.46	93.10	100.00	86.90
LDA2	e_k	8.00	14.08	0.00	0.00	8.280
	A_c	92.00	85.92	100.00	100.00	91.72
QDA1	e_k	8.00	9.86	3.45	5.00	7.59
	A_c	92.00	90.14	96.55	95.00	92.40
QDA2	e_k	12.00	12.68	6.90	10.00	11.03
	A_c	88.00	87.32	93.10	90.00	88.97

The average classification accuracy of the cross validation can be observed to be generally lower than that of the training performance for all DA model cases, as presented in figure 15. The loss in performance is due to the decrease in the training set following the LOOCV procedure, thus limiting the model learning process.

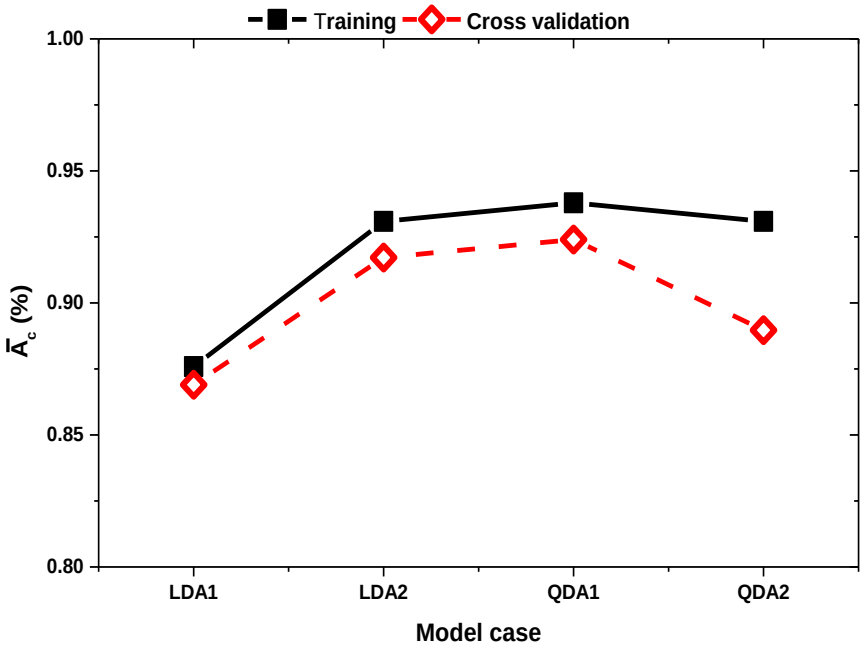

Fig.15: Comparison between the training and cross validation average classification accuracy for each DA model case

Figure 16 presents the average loss in accuracy of each DA model case such that LDA1 shows average losses at 0.69%, LDA2 at 1.37%, QDA1 at 1.39% and QDA2 at 4.12%. According to the trend, it can be inferred that model stability decreases with increasing model complexity. This is such that the most stable model (LDA1) can be regarded as the simplest model (linear with 2 features), while the least stable model (QDA2) can be considered the most complex (quadratic with 4 features).

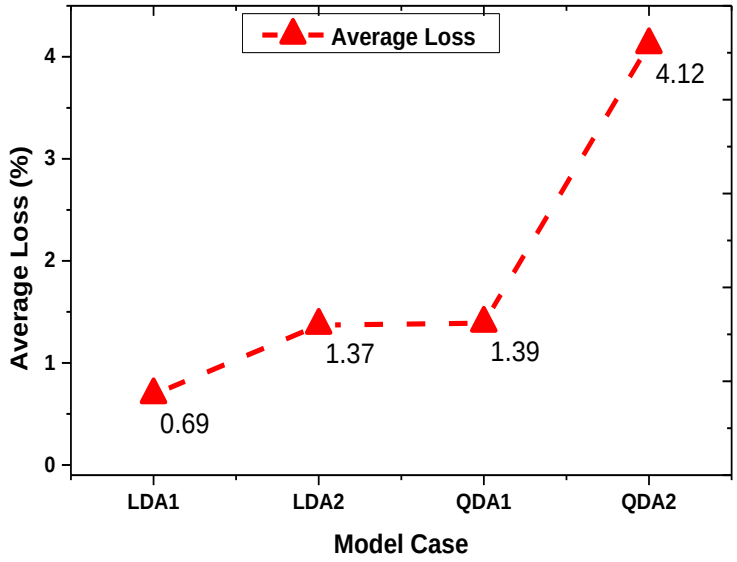

Fig. 16: Average performance losses for each DA model case

It is common to rank the performances of each model case according to classification accuracy and model stability. Good model stability with high average classification accuracy is an indication of a good bias-variance trade off. In addition, the model should also provide valid prediction of test data, defined as the unknown data set.

4.9. Model Performance testing

Figure 17(a-d) presents the posterior probability plots for the test data for each DA model case, with good separation of observations of all cases. However, this does not always reflect the correct prediction of each model case. The posterior probabilities for the LDA1 and LDA2 model cases in figures 17(a) and (b) indicate similar misclassification of only one of the slug flow observations (observation 6), which is predicted as the bubble flow regime. All other observations are correctly classified.

(a)

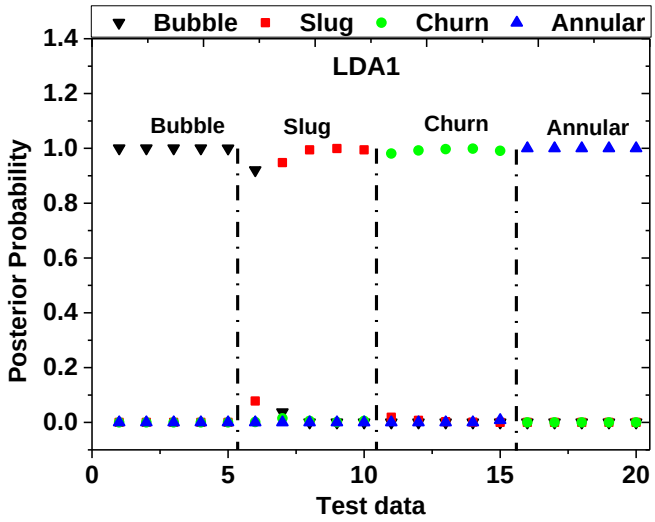
Bubble
Slug
Churn
Annular
LDA1
Bubble
Slug
Churn
Annular
Posterior Probability
Test data

(b)

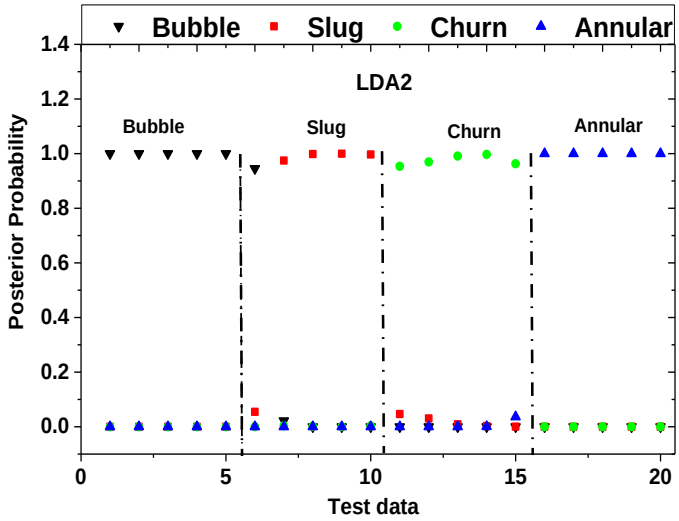
Bubble
Slug
Churn
Annular
LDA2
Bubble
Slug
Churn
Annular
Posterior Probability
Test data

(c)

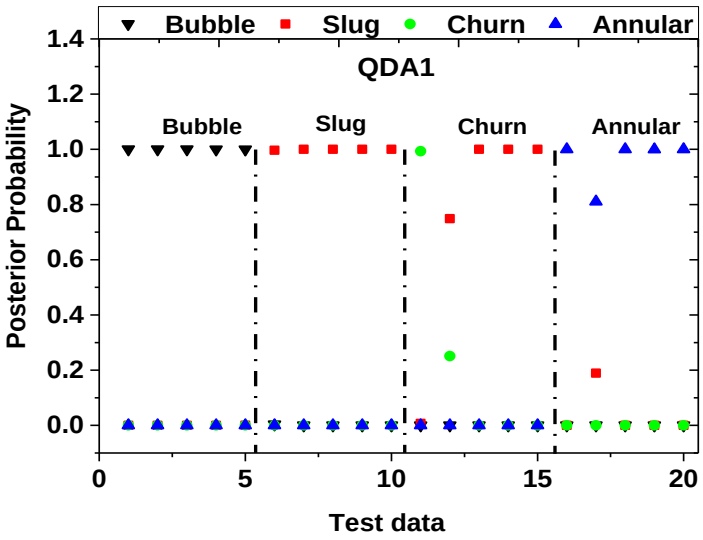
Bubble
Slug
Churn
Annular
QDA1
Bubble
Slug
Churn
Annular
Posterior Probability
Test data

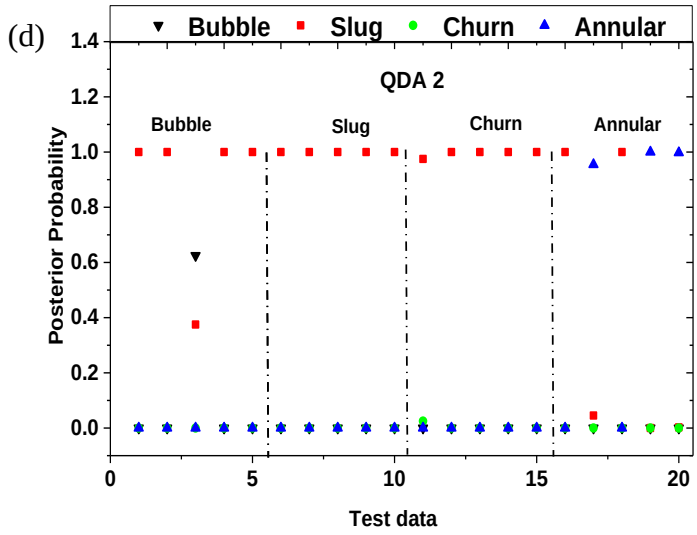

Fig. 17: Posterior probability plots of the test data set for model cases (a) LDA1 (b) LDA2 (c) QDA1 (d) QDA 2

The posterior probability plot for QDA1 in figure 17(c) indicates misclassifications of three observations (13, 14 and 15) in the churn flow regime range as slug flow regimes and correct classifications of the observations for the bubble, slug and annular flow regimes. The QDA2 model case in figure 17(d) misclassifies four out of the five bubble flow observations (1,2,4 and 5) as slug flow regime, which leaves observation 3 as the only correctly classified flow condition in the bubble flow range. More so, misclassification of all observations in the churn flow range can be observed including three out of five for the annular flow range (17, 19, 20). The incorrect predictions made by the QDA2 model case are mainly due to overfitting during model training that skews its functions to predict the slug flow regime.

Table 7 presents results of the test classification accuracies of each DA model case. The results show that LDA1 and LDA2 both perform at 95% average accuracy, while QDA1 performed at 80% and QDA2 performed at 45%. The LDA model cases are regarded as the superior model cases based on the test data considered, followed by the QDA 1 and QDA2 models. This rank of performances further establishes the fact that increasing model stability relates to increases in model prediction.

Table 7. Summary of test classification accuracy

Model Case	Bubble	Slug	Churn	Annular	$\bar{A}_c$
LDA 1	100.00%	80.00%	100.00%	100.00%	95.00%
LDA 2	100.00%	80.00%	100.00%	100.00%	95.00%
QDA 1	100.00%	100.00%	20.00%	100.00%	80.00%
QDA 2	20.00%	100.00%	0.00%	60.00%	45.00%

5. Conclusions

The results of this study demonstrate that discriminant analysis of selected features from a non-intrusive optical sensor response can be used to provide valid flow regime identification. The selection of two feature groups for the training of both the linear and quadratic discriminant analysis models (LDA1, LDA2, QDA1 and QDA2) provides a basis to test model stability and accuracy in relation to the prediction of two-phase flow structure. The training of the model cases highlights the complexities associated with predicting the slug and churn flow regimes, due to the similarity of their flow structures. A possible solution to this is the inclusion of the percentage counts of the calibrated responses for water and air in feature group 2, which can be seen to improve the separation of the posterior probabilities for the churn flow regime. This suggests that they do provide some discriminatory value, but it is not clear from the test data how this affects model accuracy. The improved flexibility of QDA also provides better separation of the posterior probabilities for the slug and churn flow regime compared to LDA. However, the improved separation of the posterior probabilities does not lead to improvements in the classification accuracy of these flow regimes due to the models being skewed to predict slug flow as a consequence of the overfitting of the discriminant functions. It may be that improvements to the model stability of the QDA1 and QDA2 model cases can be made using a larger data set for training. Cross validation of the training data produces a lower average accuracy for all of the model cases and confirms that model stability improves with model simplicity. Based on the test data runs, the LDA model cases are considered superior to the QDA due to their higher average classification accuracy and improved model stability. Further to this, LDA1 can be considered the most suitable model case for flow regime identification due its simple and robust nature, demonstrated by its low average performance loss from the cross validation. Improving classification accuracy between the slug and churn flow regimes and also model stability in general would be a useful focus for further work. Investigating the more chaotic flow structures associated with larger pipe diameters would also be an interesting focus for future studies.

Acknowledgments

The authors express their gratitude to the School of Engineering, London South Bank University for funding this research via the LSBU Doctoral Scholarship Scheme. The authors also thank the support of Mr. Medi Zahir (electronics lab technician) and Mr. Charles Coster (chemical laboratory technician) for their expert advice and support on the rig build and sensor setup.

References

[1] Kaichiro, M., and Ishii, M., 1984, "Flow Regime Transition Criteria for Upward Two-Phase Flow in Vertical Tubes," Int. J. Heat Mass Transf., **27**(5), pp. 723–737.

[2] Nicklin, D. J., 1962, "Two-Phase Flow in Vertical Tubes, Trans," Inst. Chem. Engr., **40**(1), pp. 61–68.

[3] Spedding, P. L., Woods, G. S., Raghunathan, R. S., and Watterson, J. K., 1998, "Vertical Two-Phase Flow," Chem. Eng. Res. Des., **76**(July), pp. 628–634.

[4] Oshinowo, T., and Charles, M. E., 1974, "Vertical Two-phase Flow Part I. Flow Pattern Correlations," Can. J. Chem. Eng., **52**(1), pp. 25–35.

[5] Ruixi, D., Da, Y., Haihao, W., Jing, G., Ying, L., Tong, Z., and Lijun, Z., 2013, "Optical Method for Flow Patterns Discrimination, Slug and Pig Detection in Horizontal Gas Liquid Pipe," Flow Meas. Instrum., **32**, pp. 96–102.

[6] S, A., J, A., M, V., Das, S. K., and Balakrishnan, A. R., 2016, "Two Phase Flow Regime Identification Using Infrared Sensor and Volume of Fluids Method," Flow Meas. Instrum.

[7] Sarkodie, K., Fergusson-Rees, A., and Diaz, P., 2018, "A Review of the Application of Non-Intrusive Infrared Sensing for Gas–Liquid Flow Characterization," J. Comput. Multiph. Flows, **10**(1).

[8] Berthold, J. W., Reed, S. E., and Nash, C. A., 1994, "Fibre Optic Sensor System for Void Fraction Measurement in Aqueous Two-Phase Fluids," Flow Meas. Instrum., **5**(1), pp. 3–13.

[9] Keska, J. K., and BE, W., 1999, "Experimental Comparison of Flow Pattern Detection Techniques for Air-Water Mixture Flow," Exp. Therm. Fluid Sci., **19**, pp. 1–12.

[10] Bertani, C., De Salve, M., and Malandrone, M., 2010, *State-of-Art and Selection of*

Techniques in Multiphase Flow Measurement.

[11] Elperin, T., and Klochko, M., 2002, "Flow Regime Identification in a Two-Phase Flow Using Wavelet Transform," Exp. Fluids, **32**, pp. 674–682.

[12] Chakrabarti, D. P., Das, G., and Das, P. K., 2007, "Identification of Stratified Liquid-Liquid Flow through Horizontal Pipes by a Non-Intrusive Optical Probe," Chem. Eng. Sci., **62**(7), pp. 1861–1876.

[13] Euh, D. J., and Song, C.-H., 2010, "An Application of the Wavelet Analysis Technique for the Objective Discrimination of Two-Phase Flow Patterns," Int. J. Multiph. Flow, **36**(9), pp. 755–768.

[14] Brunton, S. L., Noack, B. R., and Koumoutsakos, P., 2020, "Machine Learning for Fluid Mechanics," Annu. Rev. Fluid Mech., **52**, pp. 477–508.

[15] Yan, H., Liu, Y. H., and Liu, C. T., 2004, "Identification of Flow Regimes Using Back-Propagation Networks Trained on Simulated Data Based on a Capacitance Tomography Sensor," Meas. Sci. Technol., **15**(2), p. 432.

[16] Shaban, H., and Tavoularis, S., 2014, "Measurement of Gas and Liquid Flow Rates in Two-Phase Pipe Flows by the Application of Machine Learning Techniques to Differential Pressure Signals," Int. J. Multiph. Flow, **67**.

[17] Xu, Y., and Goodacre, R., 2018, "On Splitting Training and Validation Set: A Comparative Study of Cross-Validation, Bootstrap and Systematic Sampling for Estimating the Generalization Performance of Supervised Learning," J. Anal. Test., **2**(3), pp. 249–262.

[18] Nnabuife, S. G., Pilario, K. E. S., Lao, L., Cao, Y., and Shafiee, M., 2019, "Identification of Gas-Liquid Flow Regimes Using a Non-Intrusive Doppler Ultrasonic Sensor and Virtual Flow Regime Maps," Flow Meas. Instrum., **68**, p. 101568.

[19] Hastie, T., Tibshirani, R., Friedman, J., and Franklin, J., 2005, "The Elements of Statistical Learning: Data Mining, Inference and Prediction," Math. Intell., **27**(2), pp. 83–85.

[20] Duda, R. O., Hart, P. E., and Stork, D. G., 2012, *Pattern Classification*, John Wiley & Sons.

[21] Hiraoka, K., Hamahira, M., Hidai, K., Mizoguchi, H., Mishima, T., and Yoshizawa, S.,

2001, “Fast Algorithm for Online Linear Discriminant Analysis,” IEICE Trans. Fundam. Electron. Commun. Comput. Sci., **84**(6), pp. 1431–1441.

[22] Tharwat, A., 2016, “Linear vs. Quadratic Discriminant Analysis Classifier: A Tutorial,” Int. J. Appl. Pattern Recognit., **3**(2), pp. 145–180.

[23] Tharwat, A., Gaber, T., Ibrahim, A., and Hassanien, A. E., 2017, “Linear Discriminant Analysis: A Detailed Tutorial,” AI Commun., **30**(2), pp. 169–190.

[24] Ameel, B., De Kerpel, K., Caniere, H., T’Joen, C., Huisseune, H., and De Paepe, M., 2012, “Classification of Two Phase Flows Using Linear Discriminant Analysis and Expectation Maximization Clustering of Video Footage,” Int. J. Multiph. Flow, **40**, pp. 106–112.

[25] Li, H., Ji, H., Huang, Z., Wang, B., Li, H., and Wu, G., 2016, “A New Void Fraction Measurement Method for Gas-Liquid Two-Phase Flow in Small Channels,” Sensors, **16**(2), p. 159.

[26] Wu, W., Mallet, Y., Walczak, B., Penninckx, W., Massart, D. L., Heuerding, S., and Erni, F., 1996, “Comparison of Regularized Discriminant Analysis Linear Discriminant Analysis and Quadratic Discriminant Analysis Applied to NIR Data,” Anal. Chim. Acta, **329**(3), pp. 257–265.

[27] Wu, B., Firouzi, M., Mitchell, T., Rufford, T. E., Leonardi, C., and Towler, B., 2017, “A Critical Review of Flow Maps for Gas-Liquid Flows in Vertical Pipes and Annuli,” Chem. Eng. J., **326**, pp. 350–377.

[28] Tomiyama, A., Celata, G. P., Hosokawa, S., and Yoshida, S., 2002, “Terminal Velocity of Single Bubbles in Surface Tension Force Dominant Regime,” Int. J. Multiph. Flow, **28**(9), pp. 1497–1519.

[29] Aoyama, S., Hayashi, K., Hosokawa, S., and Tomiyama, A., 2016, “Shapes of Ellipsoidal Bubbles in Infinite Stagnant Liquids,” Int. J. Multiph. Flow, **79**, pp. 23–30.

[30] Ishii, M., and Chawla, T. C., 1979, “Local Drag Laws in Dispersed Two-Phase Flow,” STIN, **80**, p. 25631.

[31] Dutra, G., Martelli, C., Da Silva, M. J., Patyk, R. L., and Morales, R. E. M., 2017, “Air Flow Detection in Crude Oil by Infrared Light,” Sensors, **17**(6), p. 1278.

[32] Taitel, Y., Bornea, D., and Dukler, A. E., 1980, “Modelling Flow Pattern Transitions

for Steady Upward Gas-liquid Flow in Vertical Tubes," AIChE J., **26**(3), pp. 345–354.

[33] Guet, S., Ooms, G., and Oliemans, R. V. A., 2002, "Influence of Bubble Size on the Transition from Low-Re Bubbly Flow to Slug Flow in a Vertical Pipe," Exp. Therm. Fluid Sci., **26**(6–7), pp. 635–641.

[34] Das, R. K., and Pattanayak, S., 1994, "Bubble to Slug Flow Transition in Vertical Upward Two-Phase Flow through Narrow Tubes," Chem. Eng. Sci., **49**(13), pp. 2163–2172.

[35] Brauner, N., and Barnea, D., 1986, "Slug/Churn Transition in Upward Gas-Liquid Flow," Chem. Eng. Sci., **41**(1), pp. 159–163.

[36] Costigan, G., and Whalley, P. B., 1997, "Slug Flow Regime Identification from Dynamic Void Fraction Measurements in Vertical Air-Water Flows," Int. J. Multiph. Flow, **23**(2), pp. 263–282.

[37] Ishii, M., and Grolmes, M. A., 1975, "Inception Criteria for Droplet Entrainment in Two-phase Concurrent Film Flow," AIChE J., **21**(2), pp. 308–318.

[38] Whalley, P. B., 1974, "Experimental Wave and Entrainment Measurements in Vertical Annular Two-Phase Flow," *Multi-Phase Flow Systems Symp., Strathcylde., 1974*.

[39] Barnea, D., 1987, "A Unified Model for Predicting Flow-Pattern Transitions for the Whole Range of Pipe Inclinations," Int. J. Multiph. Flow, **13**(1), pp. 1–12.

[40] Maugis, C., Celeux, G., and Martin-Magniette, M.-L., 2011, "Variable Selection in Model-Based Discriminant Analysis," J. Multivar. Anal., **102**(10), pp. 1374–1387.

[41] Yanjun, Z., 2015, "A Novel Identification Method of Two Phase Flow Based on LDA Feature Extraction and GRNN in ERT System," *5th International Symposium on Knowledge Acquisition and Modeling (KAM 2015)*, Atlantis Press.